

Tiling artifacts and trade-offs of feature normalization in the segmentation of large biological images

Elena Buglakova¹, Anwai Archit², Edoardo D’Imprima^{1,4}, Julia Mahamid¹,
Constantin Pape^{2,3}, Anna Kreshuk¹

¹ European Molecular Biology Laboratory, Heidelberg

² Institute of Computer Science, University of Göttingen

³ Cluster of Excellence ‘Multiscale Bioimaging: from Molecular Machines to Networks of Excitable Cells’
(MBExC), Georg-August-University Göttingen

⁴ IRCCS Humanitas Research Hospital, Milan

Abstract

Segmentation of very large images is a common problem in microscopy, medical imaging or remote sensing. The problem is usually addressed by sliding window inference, which can theoretically lead to seamlessly stitched predictions. However, in practice many of the popular pipelines still suffer from tiling artifacts. We investigate the root cause of these issues and show that they stem from the normalization layers within the neural networks. We propose indicators to detect normalization issues and further explore the trade-offs between artifact-free and high-quality predictions, using three diverse microscopy datasets as examples. Finally, we propose to use BatchRenorm as the most suitable normalization strategy, which effectively removes tiling artifacts and enhances transfer performance, thereby improving the reusability of trained networks for new datasets.

1. Introduction

Segmentation is an essential first step of pipelines in biological image analysis, a diverse domain of computer vision that enables automated quantification for various types of microscopy images. While this domain has benefited a lot from the developments in natural image analysis, it also poses unique challenges. Investigation of biological diversity, discovery of unexpected phenotypes and development of novel imaging protocols leads to high variability of datasets. This explains the popularity of human-in-the-loop approaches to segmentation, where a small amount of data is either annotated from scratch or from the output of pre-trained models [1, 22, 26], then a new model is either trained from scratch or fine-tuned. After that the next rounds of correction and training happen, until the desired quality is

reached. Being able to quickly train a smaller model for an unseen image type is crucial in this setting.

Another important feature of biological images, especially for volumetric imaging, is their large size. Electron microscopy volumes for connectomics [6] or light sheet microscopy volumes [20] can reach the scale of multiple terabytes. It is routine to work with 10-100 GB images of $\sim 1000^3$ pixels, which exceed GPU memory.

As shown in Fig. 1, during training random patches are sampled from the annotated images and combined into a batch. During inference/evaluation, the image is split into a grid of tiles which are predicted independently and then stitched back to form the full prediction. Here we refer both to 2D and 3D image patches as tiles. In this setup the size of the tiles is limited from above by GPU memory and from below by the receptive field of the network [21]. Typical tile size is around $96 \times 96 \times 96 - 256 \times 256 \times 256$ pixels and the training batch size is 2-3 tiles per batch. During inference it is not necessary to store gradients, therefore either tile size or batch size can be larger.

Tile-wise prediction and stitching might look like a purely technical step, however for microscopy patch sampling and stitching can significantly affect prediction quality and create artifacts. In contrast, big natural image datasets, such as ImageNet [5], CityScapes [4] and SAM dataset [14], usually contain relatively small 2D images, making tiling and stitching unnecessary, as well as allowing for larger batch size.

It has been shown that seamless stitching with CNNs is possible if edge effects are taken into account [17]. For CNNs only a limited area of the input image called the receptive field affects the prediction value in a given pixel [16]. Pixels on the edge of the tile do not get full context for prediction, resulting in a mismatch between neighboring tiles. To deal with this issue the tiles are sampled

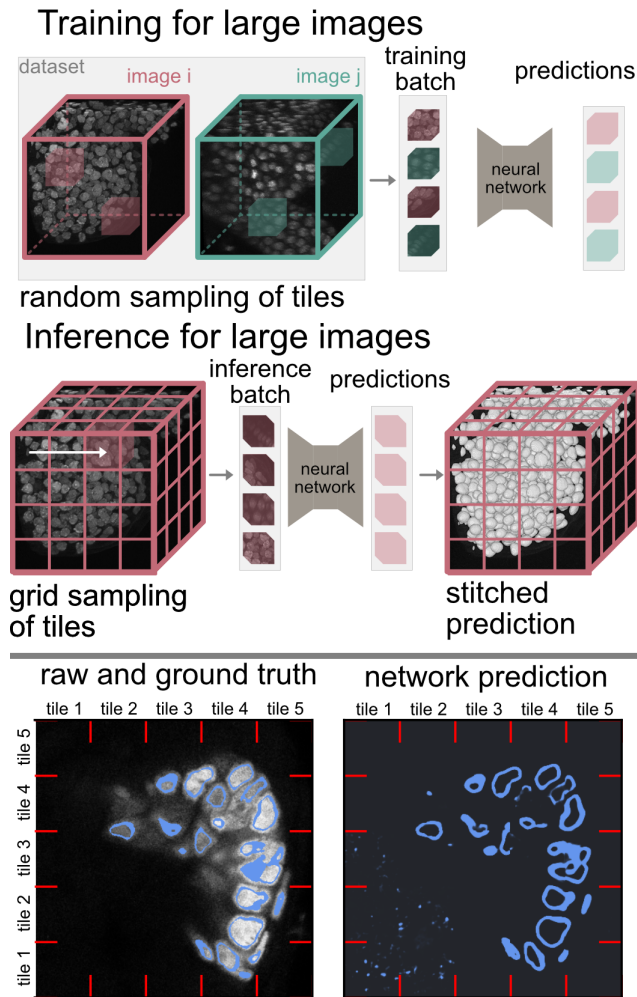


Figure 1. Illustration of the pipeline for processing images larger than GPU memory: random sampling of tiles during training and sliding window inference. Example of artifacts caused by tiling: hallucinations in the low signal areas and discontinuous predictions at the tile borders.

with overlap and only the central part of each tile is used for stitching. We refer to the removed area as halo. We find that even with sufficient halo sliding window inference can cause tiling artifacts manifesting in two ways: as abrupt discrepancy between predictions in neighboring tiles or as background hallucinations, as shown in Fig. 1 and Fig. 2. This problem is rarely discussed but it affects many widely used tools, including nnU-Net [13], a popular baseline method for biomedical image segmentation.

A common way to deal with the tiling artifacts is to apply additional postprocessing, for example, to average neighboring tiles with gaussian weights to avoid discontinuous predictions [13], or to use additional thresholding by intensity and filtering by the object size to remove artifacts in

the background like in the Fig. 1. However, adding heuristic postprocessing steps makes the whole pipeline harder to use and apply to new datasets. Moreover, we show that tiling artifacts become more pronounced in the transfer setting, further reducing reusability of the trained networks.

According to our findings, the main cause of the artifacts is the tile-wise feature normalization inside the network. If InstanceNorm [23] is used in the CNN architecture, both during training and evaluation the statistics of the current input are used for normalization. This makes predictions for every pixel dependent on the content of the whole tile, therefore the limited receptive field assumption becomes invalid and, regardless of the size of the halo, it is impossible to make the stitching seamless.

Unlike InstanceNorm, another popular normalization method BatchNorm [12] uses the statistics of the current input during training but switches to saved running average statistics in the evaluation mode, allowing to achieve seamless stitching. However, we show that the performance of the network drastically reduces in evaluation mode compared to training mode because the statistics used during training are not stable with small batch size, making the running average not representative of the statistics of individual batches. This effect has previously been observed for natural image classification [10, 11], but we find it to be significantly more pronounced in biological image segmentation.

In this work we demonstrate the trade-off between the artifact-free stitching ensured by the global normalization with BatchNorm and prediction quality achieved by tile-wise normalization with InstanceNorm. We suggest BatchRenorm [11] which uses the same global normalization statistics both during training and inference as a solution which produces artifact-free predictions without compromising on the prediction quality.

In summary, we make the following contributions:

- We show the existence of a normalization trade-off in segmentation of large biological images: using tile-wise statistics for feature normalization in the network during inference (InstanceNorm) leads to tiling artifacts even if edge effects were taken into consideration. Using tile-wise statistics in training and global accumulated statistics during inference (BatchNorm) leads to an unexpected difference between network performance during training and inference due to small batch size and high variability of the data;
- We suggest metrics for detecting normalization issues in networks used for sliding window inference pipelines: **tile mismatch** and **train/eval disparity**;
- We propose to use the **Batch Renormalization** method to achieve seamless stitching without sacrificing prediction accuracy to the train/eval disparity;
- We validate our findings on three volumetric biological

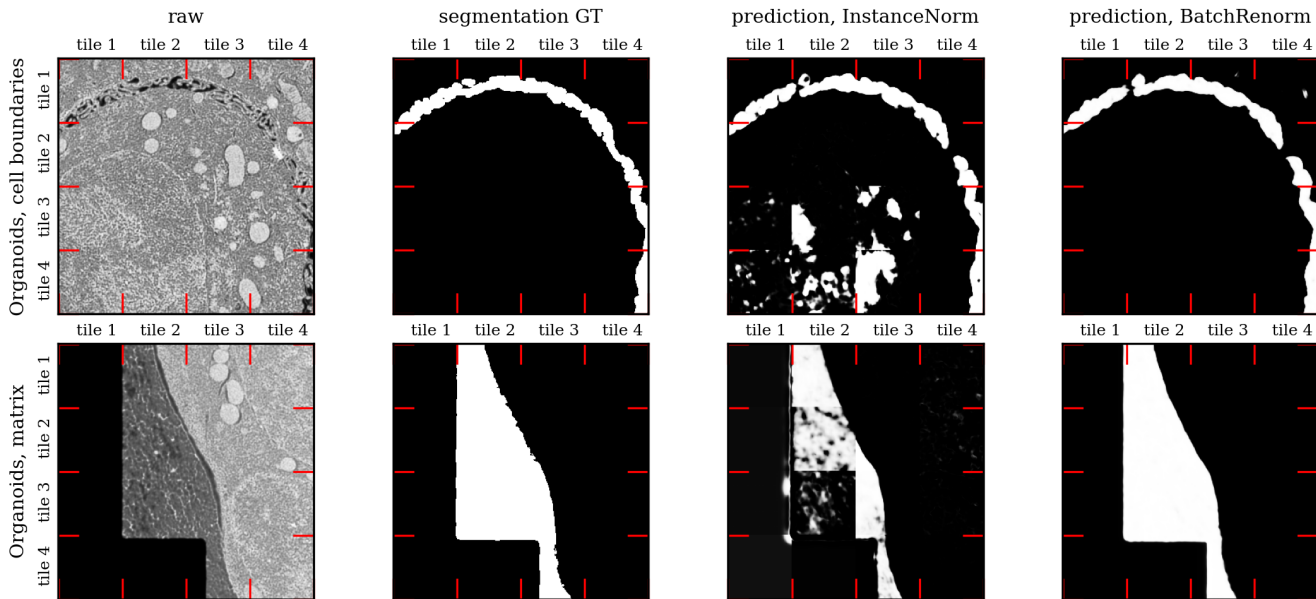


Figure 2. Examples of predictions with and without tiling artifacts

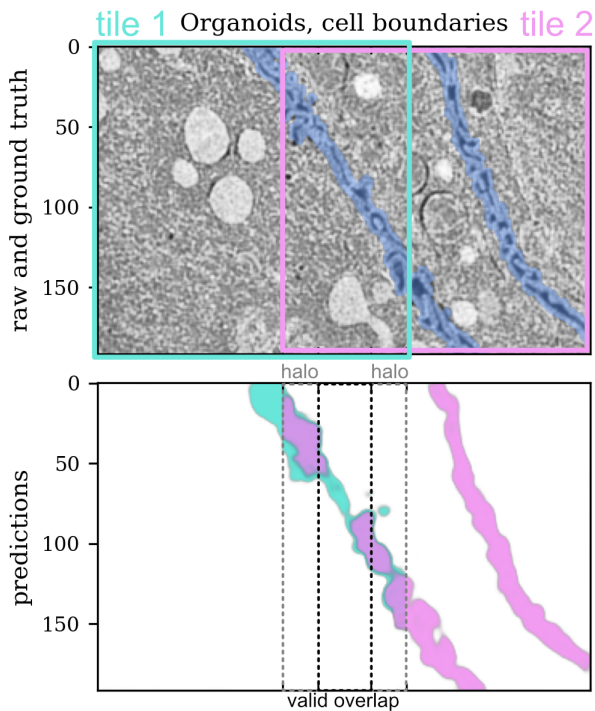


Figure 3. Illustration of the tile mismatch metric.

datasets, with two network architectures: CNN-based 3D U-Net and ViT-based UNETR.

2. Related work

Sliding window inference is used in different domains, including medical [19, 24], biological [8] and aerial [9] image analysis. It was shown that receptive field (RF) [15, 16] plays a key role in the seamless stitching [17]. Often in case of dense prediction the input and output have the same size thanks to the zero-padding in convolutional layers, so the coordinates in both spaces can be used interchangeably. For the output pixels which are closer to the edge of the tile than $\frac{1}{2}RF$ part of the input values within the receptive field is replaced by zeros, creating mismatch in the predictions between tiles. Proposed solution is to crop the prediction and only use the part of the output where each pixel has full context for stitching. The minimal sufficient size of the cropped area is $\frac{1}{2}RF$. The same concept was discussed from the point of view of translational equivariance [9, 21]. Although convolutions and pooling are translation-equivariant, zero-padding makes the CNN overall lose this property. With valid convolutions the size of the output is smaller than the input but it allows to keep the translational equivariance and therefore seamless stitching.

In practice many pipelines using sliding window inference do not aim to completely eliminate the tiling artifacts but rather minimize them by using the largest possible tile size in inference and averaging. For example, nnU-Net [13] and Cellpose [22] compute weighted average of the tiles, with the weight decreasing from 1 in the middle of the tile to 0 at the border, smoothing the border between tiles.

These recommendations help against the discontinuity in predictions caused by edge effects but our experiments

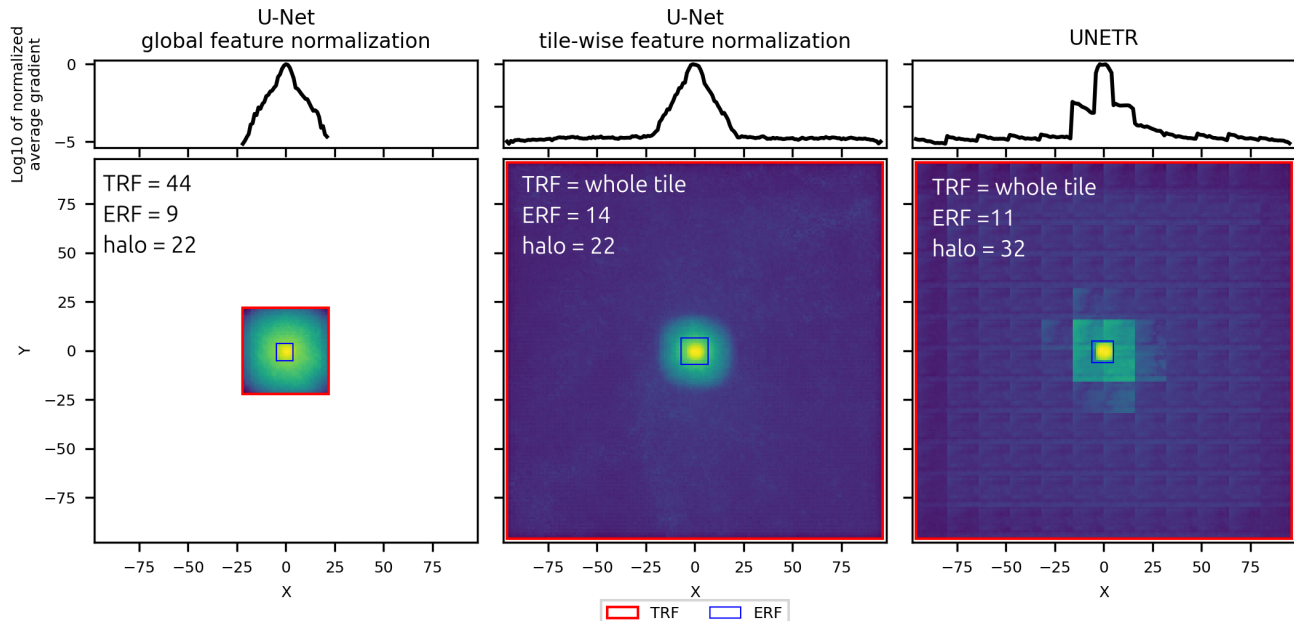


Figure 4. Receptive field, shown as Log10 of mean gradient of the central pixel output with respect to the input

show that even in the valid convolution area predictions do not necessarily match (see Fig. 3). In addition, this does not explain hallucination-like artifacts in the background like in Fig. 1. It has been shown that prediction accuracy can depend significantly on the tile size [3, 18]. To our knowledge, the connection between these effects and feature normalization inside the network was not studied before.

3. Methods

This section is structured as follows: we define how we perform sliding window inference and which normalization strategies we consider. We then propose two metrics that can identify normalization issues within the network, pointing out both tiling artifacts (“tile mismatch” metric) and performance drop in evaluation mode (“train/eval disparity” metric).

3.1. Sliding window inference with halo

Input data can be a 2D image or a 3D volume with one or multiple channels. Here both images and volumes are referred to as images. For inference the image is split into a grid of tiles, incomplete tiles are padded with zeros. The stitched prediction is calculated from by tile-wise predictions. To ensure that observed tiling artifacts were not caused by edge effects, we calculated theoretical (TRF) and effective receptive field (ERF) of the networks following [15]. We define TRF as all pixels which belong to the computation graph for the target pixel in the output space. During sliding window inference the overlap was set to the size of halo, minimizing the number of tiles needed to cover

the whole volume. The halo part of the tile was completely removed so there was no averaging of predictions or other postprocessing.

3.2. Normalization strategies

Normalization can be inserted in two parts of the pipeline: preprocessing of the input data and feature map normalization inside the network.

3.2.1. Input normalization

Quantile normalization with $q_{min} = 0.01$ and $q_{max} = 0.98$ and clipping to $[0..1]$ were applied to each image as a whole to convert the data type and value range from the microscope output to *float32* and $[0..1]$ range. In addition to the global normalization, quantile normalization can be applied to each tile separately to make the input of the network always have the same range and make tiles more comparable. Based on this we considered two strategies:

- *Global*: quantile normalization only of the whole image.
- *Tile-wise*: quantile normalization of each sampled tile, both during training and during inference.

3.2.2. Feature normalization

General formula for the normalization operation with input x , output y is:

$$y = \frac{x - \mu}{\sqrt{\sigma^2 + \epsilon}},$$

where μ and σ are normalization parameters and ϵ is a small constant used for numerical stability. Parameters μ and σ can be estimated directly from the input $\mu = E[x]$ and

$\sigma^2 = \text{Var}[x]$, where average can be taken either over each sample independently or over the whole batch. Alternatively, global normalization parameters independent of the current input can be used. A common strategy is to estimate the parameters as a running average over multiple samples: $p_{new} = (1 - \text{momentum}) \times p_{old} + \text{momentum} \times p_t$. The update speed is determined by the *momentum*.

- **BatchNorm** [12] Training: use statistics of the current batch and collect running average. Inference: use saved running average.
- **InstanceNorm** [23] Both training and inference: use statistics of each input sample. In Pytorch this behavior can be changed by setting `track_running_stats=True`. Then during inference the statistics collected during training will be utilized, same as in **BatchNorm**.
- **BatchRenorm** [11] Both training and inference: use running average statistics.
- **Identity Skip** feature normalization.

3.3. Proposed evaluation metrics

Train/eval disparity When global normalization with running average statistics is used during inference, a disparity can arise between the predictions of the same tile in train and eval mode as the train mode always uses statistics of the current batch. This disparity is an indicator of a potential drop in performance which is not related to model overfitting. To measure it quantitatively, we introduce the following metric:

$$\text{train/eval disparity} = 1 - \text{Dice}(P_{\text{train}}, P_{\text{eval}}),$$

where P_{train} is the prediction done with `model.train()` and P_{eval} - with `model.eval()`.

Tile mismatch

Quantification of tiling artifacts is challenging because their magnitude depends on the similarity of the content of neighboring tiles in different parts of the image. We propose to split the image into overlapping tiles and compare the predictions in the overlap areas. To avoid edge effects, we only take the valid part of the overlap, as shown in Fig. 3. The following metrics are proposed:

$$\text{max dist} = \max_{i=1}^M (|O_{i1} - O_{i2}|)$$

$$\text{tile mismatch} = \text{median}_{i=1}^M (1 - \text{Dice}(O_{i1}, O_{i2})),$$

where O_{i1} and O_{i2} are predictions in the valid overlap region in tile i and M is number of sampled tiles. In *max dist* max is taken over all channels and all tiles, making it an indicator of whether given setup produces tiling artifacts. In cases when *max dist* = 0 we explicitly

report "no" instead of *tile mismatch* to emphasize that the predictions perfectly match. *tile mismatch* is calculated per channel and characterizes the magnitude of the artifacts.

4. Experiments

4.1. Datasets

The datasets were chosen to demonstrate the common challenges of microscopy segmentation such as large image size and variability of class distributions within the volume.

organoids [7]: semantic segmentation of tissue in patient-derived colorectal cancer organoids, electron microscopy (FIB/SEM), $40 \times 30 \times 30 \text{ nm}^3$ voxel size. The volume of size $1350 \times 1506 \times 1647$ pixels was split 70/30 into train and validation dataset. Classes: cell boundaries, foreground (pixels inside the cells), extracellular matrix (space between cells and background).

plants [25]: instance segmentation of nuclei in Arabidopsis ovules, confocal fluorescent microscopy, isotropic resolution of $0.13 \mu\text{m}^3$ per pixel, 4 train volumes and 1 validation volume $\sim 500 \times 1000 \times 1000$ pixels each.

embryo [2]: instance segmentation of nuclei in mouse embryos, confocal fluorescent microscopy, isotropic resolution of $0.2 \mu\text{m}^3$ per pixel, 22 train volumes and 13 validation volumes, $\sim 600 \times 1000 \times 700$ px each.

For **plants** and **embryo** datasets the original instance segmentation groundtruth was converted to semantic segmentation of three classes: object boundaries, foreground (objects with subtracted boundaries) and background. For the **transfer setup**, networks trained for **embryo** dataset were used to segment **plants** dataset and vice versa.

4.2. Architectures

3D U-Net: 3D U-Net with 2 downsampling steps and 2 convolutional blocks per level was used for all datasets. Each convolutional block consists of a convolutional layer, a normalization layer and a non-linearity. The normalization layers in all the blocks were replaced with one of the normalization layers listed above. Tile size (192, 192, 192) was used for training and (128, 128, 128) for sliding window inference.

3D UNETR: UNETR consists of a ViT encoder and a convolutional decoder. In the encoder the volume is split into $16 \times 16 \times 16$ patches and embeddings in the ViT are normalized using `LayerNorm` after each round of attention. With `LayerNorm` all features are normalized using average and variance of the features in each patch independently. Other normalization strategies can be used in the ViT [27], but here `LayerNorm` was kept in all experiments as a standard approach. Convolutional decoder consists of 4 upsampling steps with 2 convolutional blocks at each level of the U-Net-like architecture. The normalization layers in

Table 1. U-Net results table

| Normalization layer | | | BatchNorm | BatchNorm | InstanceNorm | InstanceNorm | BatchRenorm | Identity |
|----------------------|-----------|------------|-------------|-------------|--------------|--------------|-------------|-------------|
| Input norm | | | global | tile-wise | global | tile-wise | global | global |
| Feature norm | | | global | global | tile-wise | tile-wise | global | global |
| dice, eval mode | organoids | foreground | 0.95 | 0.88 | 0.94 | 0.93 | 0.95 | 0.95 |
| | | boundaries | 0.49 | 0.15 | 0.75 | 0.75 | 0.73 | 0.72 |
| | | matrix | 0.82 | 0.61 | 0.61 | 0.61 | 0.85 | 0.83 |
| | plants | foreground | 0.85 | 0.88 | 0.89 | 0.89 | 0.89 | 0.52 |
| | | boundaries | 0.69 | 0.73 | 0.75 | 0.74 | 0.75 | 0.26 |
| | embryo | foreground | 0.66 | 0.68 | 0.67 | 0.72 | 0.74 | 0.59 |
| | | boundaries | 0.55 | 0.55 | 0.55 | 0.53 | 0.58 | 0.44 |
| dice, train mode | organoids | foreground | 0.94 | 0.93 | 0.94 | 0.93 | 0.95 | 0.95 |
| | | boundaries | 0.75 | 0.75 | 0.75 | 0.75 | 0.73 | 0.72 |
| | | matrix | 0.61 | 0.61 | 0.61 | 0.61 | 0.85 | 0.83 |
| | plants | foreground | 0.89 | 0.89 | 0.89 | 0.89 | 0.89 | 0.52 |
| | | boundaries | 0.75 | 0.74 | 0.75 | 0.74 | 0.75 | 0.26 |
| | embryo | foreground | 0.67 | 0.72 | 0.67 | 0.72 | 0.74 | 0.59 |
| | | boundaries | 0.55 | 0.52 | 0.55 | 0.53 | 0.58 | 0.44 |
| train/eval disparity | organoids | | 0.48 | 0.84 | 0 | 0 | 0 | 0 |
| | plants | | 0.17 | 0.11 | 0 | 0 | 0 | 0 |
| | embryo | | 0.37 | 0.29 | 0 | 0 | 0 | 0 |
| tile mismatch | organoids | | no | 0.03 | 0.11 | 0.11 | no | no |
| | plants | | no | 0.01 | 0.05 | 0.05 | no | no |
| | embryo | | no | 0.09 | 0.16 | 0.20 | no | no |

all the blocks were replaced with one of the normalization layers listed above.

4.3. Reported metrics

Overall prediction quality: Prediction was done on the whole volume using sliding window inference as described above. If the setup included tile-wise input normalization, each tile was normalized separately before being passed through the network. The median Dice score over all samples in the validation dataset was reported for each class.

Train/eval disparity: We report the Dice score both for training and evaluation mode to demonstrate the disparity in Tab. 1 and Tab. 2. Inference in both modes was done on the same images from the validation set, so the difference comes only from the behavior of the model in different modes and not overfitting to the training data. **Tile mismatch:** The tiles of $192 \times 192 \times 288$ px were sampled in a grid with a stride of 64 pixels to test the mismatch in the whole volume. Sampled tiles were split into two overlapping tiles of size $192 \times 192 \times 192$. Both tiles were then processed to compare the predictions in the overlapping region. Tile mismatch values for boundary channel are reported in Tab. 1, Tab. 2 and STab. 1.

Further details can be found in the Supplementary.

5. Results

5.1. Receptive field

We calculated TRF and ERF for the architectures with different normalization layers. As expected, for U-Net with the global feature normalization (BatchNorm, BatchRenorm, Identity) only a limited region around the central pixel belongs to TRF, ERF constitutes the effective receptive field only the small portion as shown in Fig. 4. For the U-Net with tile-wise feature normalization (InstanceNorm) ERF is the same, which is expected since it is determined by the parameters of the convolutional architecture, but the TRF takes the whole tile as values of all pixels in the tile make a contribution to the prediction for the central pixel via normalization. Therefore, regardless of the size of the overlap between tiles in the sliding window prediction, the stitched prediction will not be exactly seamless. In all sliding window experiments with the U-Net we used halo calculated using TRF of the U-Net with global feature normalization (Fig. 4).

For UNETR TRF also takes the whole input tile due to normalization in the convolutional decoder and the attention mechanism. The averaged gradients image Fig. 4 has a clear square pattern because in the encoder the image is downsampled by 16 and then upsampled back to the origi-

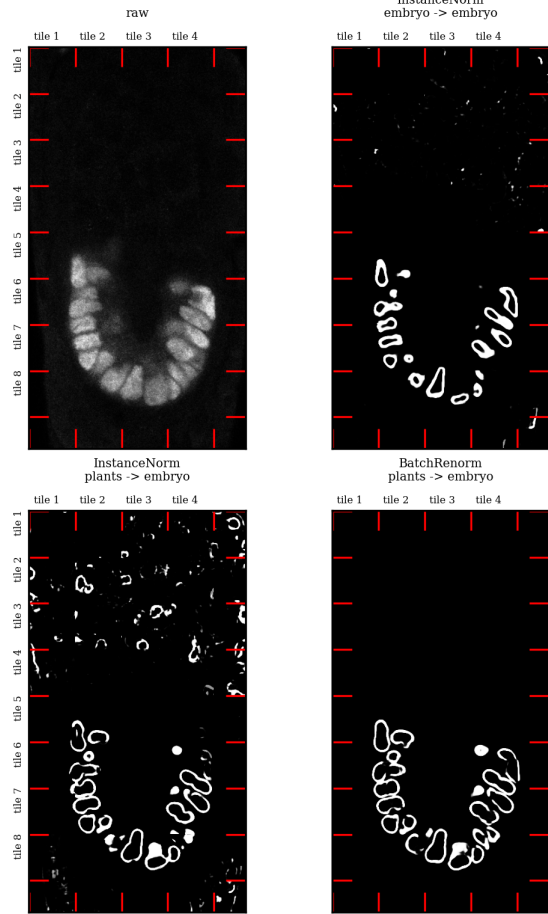


Figure 5. Tiling artifacts become more pronounced in a transfer setting. For quantitative evaluation see STab. 1.

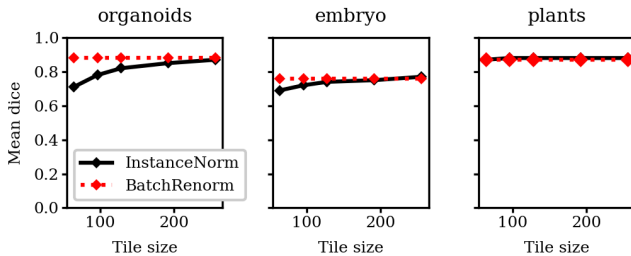


Figure 6. Performance vs tile size.

nal resolution. Despite the attention layers, ERF is the same as for the U-Net. Since only 3 central patches have large effect on the central pixel prediction, we set $halo = 32$ for all UNETR experiments (Fig. 4).

5.2. Tile-wise feature normalization with InstanceNorm causes tiling artifacts

Using InstanceNorm allows to reach high quality predictions, however the tile-wise feature normalization is a

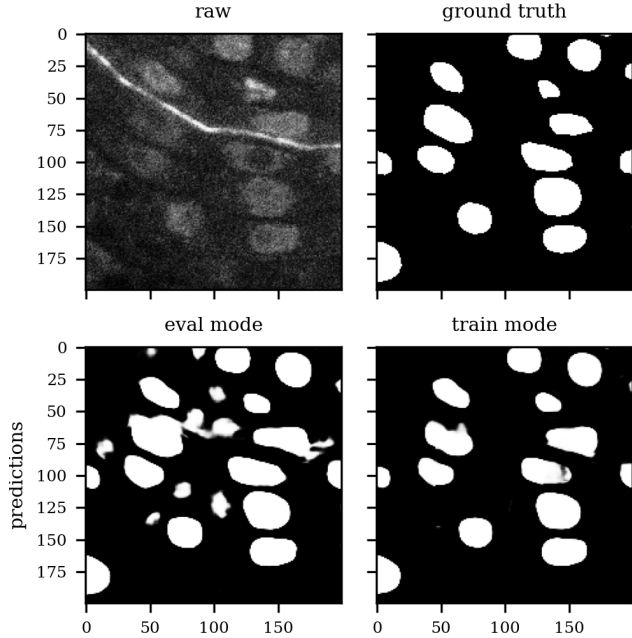


Figure 7. Example of train/eval disparity

source of artifacts both for U-Net (Tab. 1) and for UNETR (Tab. 2) as shown in Fig. 2. We observe that tile-wise input normalization (BatchNorm, tile-wise input norm) causes less severe tile mismatch than tile-wise network feature normalization (InstanceNorm, global input norm). Although it is impossible to reach completely seamless stitching with UNETR, experiments with InstanceNorm show strong tile mismatch, while global feature normalization and sufficient halo based on ERF size allow to reduce mismatch and make it almost unnoticeable.

Although InstanceNorm performs better than BatchNorm for boundaries, networks with tile-wise normalization struggle with classes which cover areas larger than the tile size, such as foreground and matrix in organoids dataset. Experiments with inference using different tile sizes Fig. 6 show that the prediction depends strongly on the tile size, reaching the best quality when the tiles become large enough for the feature distribution in each tile to reproduce the distribution in the whole image.

Fig. 5 shows how artifacts get worse in the transfer setting: the model originally trained on the embryo dataset produces less artifacts than the model transferred from the plants dataset. We observe the same effect in transfer in both directions (STab. 1).

5.3. Mismatch in batch statistics causes train and eval mode disparity for BatchNorm

Global feature normalization with BatchNorm allows to eliminate the tile mismatch but predictions for organoids boundary and other datasets are worse than with

Table 2. UNETR results table

| Norm layer | | BatchNorm | InstanceNorm | BatchRenorm | Identity |
|--------------|--|-----------|--------------|-------------|----------|
| Input norm | | global | global | global | global |
| Feature norm | | global | tile-wise | global | global |

| dice, eval mode | organoids | foreground | 0.93 | 0.89 | 0.95 | 0.91 |
|-----------------|------------|-------------|-------------|-------------|-------------|------|
| | | boundaries | 0.39 | 0.60 | 0.72 | 0.60 |
| plants | matrix | 0.03 | 0.10 | 0.87 | 0.28 | |
| | foreground | 0.84 | 0.85 | 0.85 | 0.52 | |
| embryo | boundaries | 0.64 | 0.69 | 0.66 | 0.21 | |
| | foreground | 0.67 | 0.56 | 0.67 | 0.00 | |
| | boundaries | 0.49 | 0.49 | 0.53 | 0.00 | |

| dice, train mode | organoids | foreground | 0.89 | 0.89 | 0.95 | 0.91 |
|------------------|------------|-------------|-------------|-------------|-------------|------|
| | | boundaries | 0.60 | 0.60 | 0.72 | 0.60 |
| plants | matrix | 0.10 | 0.10 | 0.87 | 0.28 | |
| | foreground | 0.85 | 0.85 | 0.85 | 0.52 | |
| embryo | boundaries | 0.69 | 0.69 | 0.66 | 0.21 | |
| | foreground | 0.56 | 0.56 | 0.67 | 0.00 | |
| | boundaries | 0.49 | 0.49 | 0.53 | 0.00 | |

| t/e disparity | organoids | 0.36 | 0 | 0 | 0 |
|---------------|-----------|----------|----------|----------|----------|
| plants | 0.20 | 0 | 0 | 0 | |
| embryo | 0.33 | 0 | 0 | 0 | |

| tile mismatch | organoids | 0.00 | 0.10 | 0.00 | 0.00 |
|---------------|-------------|-------------|------|-------------|-------------|
| plants | 0.00 | 0.00 | 0.04 | 0.00 | 0.00 |
| embryo | 0.00 | 0.00 | 0.06 | 0.00 | 0.00 |

InstanceNorm. The reason for this is the disparity between the performance of the network in train and evaluation mode. Estimation of normalization statistics with a running average in BatchNorm relies on the batch statistics being stable enough to represent the whole dataset. If batches are too small, the running average can be very different from the batch-wise statistics used during training, leading to deteriorating performance. Doing inference with the network in train mode supports this hypothesis: the performance recovers, at the cost of tiling artifacts. In our experiments train and evaluation mode predictions can be quite different, with train/eval disparity reaching 0.84 for the organoids dataset. Qualitatively, the changes in the predictions occur in the areas of low prediction certainty. For example, in Fig. 7 the eval mode differs from the train mode in the areas where the background has a bright line artifact or in the noisier areas.

This effect is not the same as the usual difference between train and evaluation performance caused by overfitting. Here, the network’s output differs even for the exact

same images thus violating the usual assumption that the prediction quality is approximately the same in train and eval mode. This issue would not be remedied by using augmentations or more training data as it does not address the high variance of statistics.

5.4. BatchRenorm corrects for train/eval disparity and provides seamless stitching

InstanceNorm avoids the statistics mismatch by always using the statistics of the input both during training and during inference at the cost of causing tiling artifacts. BatchNorm does not introduce the tiling artifacts but can lose performance due to train/eval disparity.

A potential solution is to remove the normalization altogether. In our experiments not using normalization (Identity in Tab. 1 and Tab. 2) has led to worse performance for plants dataset and similar performance for organoids and embryo. It could be possible to improve the performance of networks with no normalization by finding more suitable training parameters and reducing the learning rate, however the necessity to adjust training parameters for each dataset makes the pipeline harder to use.

Another solution is to use the same global normalization statistics both in training and in inference. Directly using running average statistics during training causes network’s weights to explode [11], which is why we propose to use Batch Renormalization method. We found that networks with BatchRenorm produce same or better predictions as InstanceNorm (Tab. 1, Tab. 2) including the transfer setup (STab. 1) while allowing for seamless stitching due to global feature normalization (last column of Fig. 2, Fig. 5).

6. Discussion

The severity of tiling artifacts depends on the data and on the tile size. For example, the tile mismatch can be negligible in case the images are very homogeneous in content and the tile size is big enough that each tile mostly reproduces the global statistics of the image, such as for plants dataset in our experiments. However, even in that case the inference performance depends on the tile size and can change unpredictably in the transfer setting, putting higher requirements on the hardware for inference and making the pipeline harder to use, especially for non-expert users. Tracing low validation accuracy to the instability in batch statistics is not straightforward either, as it is normally expected that the performance on the validation dataset should be worse than on the training data. If the training loss is low but the accuracy on validation data does not improve, it is often attributed to the insufficient amount of ground truth, however, we show that it can also be caused by train/eval disparity preventing efficient utilization of the ground truth.

Both of the described effects are highly dependent on the particular data, input normalization, sampling strategy,

postprocessing and other parameters of the image analysis pipeline. For any such pipeline, we introduce two simple metrics: *tile mismatch* and *train/eval disparity* to help determine if it has issues with normalization. Both metrics are easy to use for any sliding window inference pipeline, including other dense prediction tasks if the Dice score is replaced with another, task-appropriate metric.

We found that `BatchRenorm`, originally introduced for natural image classification, performs well for segmenting large biological images. The challenge with images larger than GPU memory is ensuring consistent normalization parameters across the entire image for seamless stitching, despite the inability to process the full image during training due to time constraints. `BatchRenorm` solves this by splitting training into two stages. First, the network is trained with `BatchNorm`. Then the normalization layer switches to using the accumulated running average statistics. In our experience it is very important that the training converges before switching and that the statistics change from tile-wise to global gradually to achieve the best final accuracy. While the `BatchRenorm` adds more hyperparameters, in our experiments the right moment to switch could easily be found from looking at the loss curves.

7. Conclusion

In this paper, we demonstrate that tiling artifacts in sliding window inference pipelines can be caused by the tile-wise feature normalization in the network. We also find that switching from tile-wise normalization in training to global normalization in evaluation can lead to even worse performance, including hallucinations, due to small batch size. As these effects strongly depend on the data and tile size, we introduce *tile mismatch* and *train/eval disparity* metrics to easily check if a specific pipeline and dataset have these issues. We propose that Batch Renormalization technique will yield artifact-free predictions even with small batch size and demonstrate its good performance through extensive experiments on various microscopy datasets and network architectures.

Acknowledgment. We would like to thank Ricardo Sánchez Loayza for helpful discussions. E.B. was supported by the Joachim Herz Foundation through an Add-on Fellowship for Interdisciplinary Life Science. E.D'I. was supported by a fellowship from the EMBL Interdisciplinary (EI4POD) program under Marie Skłodowska-Curie Actions COFUND (847543). J.M. acknowledges funding from the EMBL and the European Research Council (ERC 3DCellPhase- 760067). This work was supported by the European Commission through the Horizon Europe program (IMAGINE project, grant agreement 101094250-IMAGINE). The work of A.A. was funded by the German Research Foundation through PA 4341/2-1. C.P. received support under Germany's Excellence Strategy - EXC

2067/1-390729940. We would like to thank the EMBL IT Services Department for providing computational infrastructure and support.

References

- [1] Anwai Archit, Luca Freckmann, Sushmita Nair, Nabeel Khalid, Paul Hilt, Vikas Rajashekar, Marei Freitag, Carolin Teuber, Genevieve Buckley, Sebastian von Haaren, Sagnik Gupta, Andreas Dengel, Sheraz Ahmed, and Constantin Pape. Segment anything for microscopy. *Nature Methods*, 2025. 1
- [2] Vladyslav Bondarenko, Mikhail Nikolaev, Dimitri Kromm, Roman Belousov, Adrian Wolny, Marloes Blotenburg, Peter Zeller, Saba Rezakhani, Johannes Hugger, Virginie Uhlmann, Lars Hufnagel, Anna Kreshuk, Jan Ellenberg, Alexander van Oudenaarden, Anna Erzberger, Matthias P Lutolf, and Takashi Hiiragi. Embryo-uterine interaction coordinates mouse embryogenesis during implantation. *The EMBO Journal*, 42(17), 2023. 5
- [3] Calimanut-Ionut Cira, Miguel-Ángel Manso-Callejo, Naoto Yokoya, Tudor Sălăgean, and Ana-Cornelia Badea. Impact of tile size and tile overlap on the prediction performance of convolutional neural networks trained for road classification. *Remote Sensing*, 16(15):2818, 2024. 4
- [4] Marius Cordts, Mohamed Omran, Sebastian Ramos, Timo Rehfeld, Markus Enzweiler, Rodrigo Benenson, Uwe Franke, Stefan Roth, and Bernt Schiele. The cityscapes dataset for semantic urban scene understanding. In *Proc. of the IEEE Conference on Computer Vision and Pattern Recognition (CVPR)*, 2016. 1
- [5] Jia Deng, Wei Dong, Richard Socher, Li-Jia Li, Kai Li, and Li Fei-Fei. Imagenet: A large-scale hierarchical image database. In *2009 IEEE Conference on Computer Vision and Pattern Recognition*, pages 248–255, 2009. 1
- [6] Sven Dorkenwald, Arie Matsliah, Amy R Sterling, Philipp Schlegel, Szi-Chieh Yu, Claire E McKellar, Albert Lin, Marta Costa, Katharina Eichler, Yijie Yin, Will Silversmith, Casey Schneider-Mizell, Chris S Jordan, Derrick Brittain, Akhilesh Halageri, Kai Kuehner, Oluwaseun Ogedengbe, Ryan Morey, Jay Gager, Krzysztof Kruk, Eric Perlman, Runzhe Yang, David Deutsch, Doug Bland, Marissa Sorek, Ran Lu, Thomas Macrina, Kisuk Lee, J Alexander Bae, Shang Mu, Barak Nehoran, Eric Mitchell, Sergiy Popovych, Jingpeng Wu, Zhen Jia, Manuel A Castro, Nico Kemnitz, Dodam Ih, Alexander Shakeel Bates, Nils Eckstein, Jan Funke, Forrest Collman, Davi D Bock, Gregory S X E Jefferis, H Sebastian Seung, Mala Murthy, and FlyWire Consortium. Neuronal wiring diagram of an adult brain. *Nature*, 634(8032): 124–138, 2024. 1
- [7] Edoardo D’Imprima, Marta Garcia Montero, Sylwia Gawrzak, Paolo Ronchi, Ievgeniia Zagoriy, Yannick Schwab, Martin Jechlinger, and Julia Mahamid. Light and electron microscopy continuum-resolution imaging of 3d cell cultures. *Developmental Cell*, 58(7):616–632.e6, 2023. 5
- [8] T. Falk, D. Mai, R. Bensch, Ö. Çiçek, A. Abdulkadir, Y. Marrakchi, A. Böhm, J. Deubner, Z. Jäckel, K. Seiwald, A.

- Dovzhenko, O. Tietz, C. Dal Bosco, S. Walsh, D. Saltukoglu, T. L. Tay, M. Prinz, K. Palme, M. Simons, I. Diester, T. Brox, and O. Ronneberger. U-net – deep learning for cell counting, detection, and morphometry. *Nature Methods*, 16: 67–70, 2019. 3
- [9] Bohao Huang, Daniel Reichman, Leslie M. Collins, Kyle Bradbury, and Jordan M. Malof. Tiling and stitching segmentation output for remote sensing: Basic challenges and recommendations. *arXiv: Computer Vision and Pattern Recognition*, 2018. 3
- [10] Lei Huang, Jie Qin, Yi Zhou, Fan Zhu, Li Liu, and Ling Shao. Normalization techniques in training dnns: Methodology, analysis and application. *IEEE Transactions on Pattern Analysis and Machine Intelligence*, 45(8):10173–10196, 2023. 2
- [11] Sergey Ioffe. Batch renormalization: Towards reducing minibatch dependence in batch-normalized models. In *Advances in Neural Information Processing Systems*. Curran Associates, Inc., 2017. 2, 5, 8
- [12] Sergey Ioffe and Christian Szegedy. Batch normalization: Accelerating deep network training by reducing internal covariate shift. In *Proceedings of the 32nd International Conference on Machine Learning*, pages 448–456, Lille, France, 2015. PMLR. 2, 5
- [13] Fabian Isensee, Paul F. Jaeger, Simon A. A. Kohl, Jens Petersen, and Klaus H. Maier-Hein. nnu-net: a self-configuring method for deep learning-based biomedical image segmentation. *Nature Methods*, 18(2):203–211, 2020. 2, 3
- [14] Alexander Kirillov, Eric Mintun, Nikhila Ravi, Hanzi Mao, Chloe Rolland, Laura Gustafson, Tete Xiao, Spencer Whitehead, Alexander C. Berg, Wan-Yen Lo, Piotr Dollár, and Ross Girshick. Segment anything. In *2023 IEEE/CVF International Conference on Computer Vision (ICCV)*, pages 3992–4003, 2023. 1
- [15] Vincent Loos, Rohit Pardasani, and Navchetan Awasthi. Demystifying the effect of receptive field size in u-net models for medical image segmentation. *Journal of Medical Imaging*, 11(05), 2024. 3, 4
- [16] Wenjie Luo, Yujia Li, Raquel Urtasun, and Richard Zemel. Understanding the effective receptive field in deep convolutional neural networks. In *Advances in Neural Information Processing Systems*. Curran Associates, Inc., 2016. 1, 3
- [17] Michael Majurski and Peter Bajcsy. Exact tile-based segmentation inference for images larger than gpu memory. *Journal of Research of the National Institute of Standards and Technology*, 126, 2021. 1, 3
- [18] G. Anthony Reina, Ravi Panchumarthy, Siddhesh Pravin Thakur, Alexei Bastidas, and Spyridon Bakas. Systematic evaluation of image tiling adverse effects on deep learning semantic segmentation. *Frontiers in Neuroscience*, 14, 2020. 4
- [19] O. Ronneberger, P.Fischer, and T. Brox. U-net: Convolutional networks for biomedical image segmentation. In *Medical Image Computing and Computer-Assisted Intervention (MICCAI)*, pages 234–241. Springer, 2015. (available on arXiv:1505.04597 [cs.CV]). 3
- [20] Xiongtao Ruan, Matthew Mueller, Gaoxiang Liu, Frederik Görlitz, Tian-Ming Fu, Daniel E Milkie, Joshua L Lillvis, Alexander Kuhn, Johnny Gan Chong, Jason Li Hong, Chu Yi Aaron Herr, Wilmene Hercule, Marc Nienhaus, Alison N Killilea, Eric Betzig, and Srigokul Upadhyayula. Image processing tools for petabyte-scale light sheet microscopy data. *Nat. Methods*, 21(12):2342–2352, 2024. 1
- [21] Josef Lorenz Rumberger, Xiaoyan Yu, Peter Hirsch, Melanie Dohmen, Vanessa Emanuela Guarino, Ashkan Mokarian, Lisa Mais, Jan Funke, and Dagmar Kainmueller. How shift equivariance impacts metric learning for instance segmentation. In *2021 IEEE/CVF International Conference on Computer Vision (ICCV)*, page 7108–7116. IEEE, 2021. 1, 3
- [22] Carsen Stringer, Tim Wang, Michalis Michaelos, and Marius Pachitariu. Cellpose: a generalist algorithm for cellular segmentation. *Nature Methods*, 18(1):100–106, 2020. 1, 3
- [23] Dmitry Ulyanov, Andrea Vedaldi, and Victor Lempitsky. Instance normalization: The missing ingredient for fast stylization, 2016. 2, 5
- [24] Özgün undefinediçek, Ahmed Abdulkadir, Soeren S. Lienkamp, Thomas Brox, and Olaf Ronneberger. *3D U-Net: Learning Dense Volumetric Segmentation from Sparse Annotation*, page 424–432. Springer International Publishing, 2016. 3
- [25] Athul Vijayan, Tejasvinee Atul Mody, Qin Yu, Adrian Wolny, Lorenzo Cerrone, Soeren Strauss, Miltos Tsiantis, Richard S. Smith, Fred A. Hamprecht, Anna Kreshuk, and Kay Schneitz. A deep learning-based toolkit for 3d nuclei segmentation and quantitative analysis in cellular and tissue context. *Development*, 151(14), 2024. 5
- [26] Martin Weigert, Uwe Schmidt, Robert Haase, Ko Sugawara, and Gene Myers. Star-convex polyhedra for 3d object detection and segmentation in microscopy. In *2020 IEEE Winter Conference on Applications of Computer Vision (WACV)*, page 3655–3662. IEEE, 2020. 1
- [27] Zhuliang Yao, Yue Cao, Yutong Lin, Ze Liu, Zheng Zhang, and Han Hu. Leveraging batch normalization for vision transformers. In *2021 IEEE/CVF International Conference on Computer Vision Workshops (ICCVW)*. IEEE, 2021. 5

Supplementary materials

A. Implementation details

All experiments were implemented using MONAI¹ framework. The models were trained on a slurm cluster with NVIDIA GeForce RTX 3090 GPUs with the batch size of 1 and gradient accumulation for 8 steps, using the Adam optimizer with initial learning rate of 0.001 for 25,000 iterations. The only augmentation was flip with probability 0.5. During training tiles of size $192 \times 192 \times 192$ were sampled from the volumes randomly. Dice loss averaged over channels was used for training. Dice is not defined when the label has no non-zero pixels, therefore for tiles with empty channels the empty channels were not used in averaging.

U-Net with two downsampling steps and 32, 64 and 128 feature maps in the first, second and bottleneck levels was used. For all normalization layers that use running average to collect statistics `momentum` was set to 0.01.

UNETR encoder had $16 \times 16 \times 16$ patch size, 12 attention heads and hidden embedding size 768. Convolutional patch projection and trainable positional embedding were used, following the recommendations in the UNETR paper.

For the Batch Renormalization layer (adapted from <https://github.com/ludvb/batchrenorm>) we set $r_{max} = 3$, $d_{max} = 5$ following the original paper. The models were trained for 1000 steps for embryo and organoids datasets and 5000 steps for plants dataset with $r = 1$ and $d = 0$, then the parameters were linearly increased to r_{max} and d_{max} over 1000 steps.

¹<https://monai.io>

Table 1. U-Net transfer between plants and embryo datasets. Values in gray correspond to the non-transfer experiments.

| Normalization layer | | BatchNorm | BatchNorm | InstanceNorm | InstanceNorm | BatchRenorm | Identity | |
|---------------------|-----------------|---------------------|------------|--------------|--------------|---------------------|---------------------|-----------|
| Input norm | | global | tile-wise | global | tile-wise | global | global | |
| Feature norm | | global | global | tile-wise | tile-wise | global | global | |
| Target | Source | plant | embryo | plant | embryo | plant | embryo | |
| | dice, eval mode | plants | foreground | 0.85 0.36 | 0.88 0.42 | 0.89 0.50 | 0.89 0.53 | 0.89 0.50 |
| boundaries | | | 0.69 0.11 | 0.73 0.14 | 0.75 0.27 | 0.74 0.22 | 0.74 0.29 | 0.26 0.25 |
| embryo | | foreground | 0.51 0.66 | 0.51 0.68 | 0.54 0.67 | 0.54 0.72 | 0.59 0.74 | 0.45 0.59 |
| | | boundaries | 0.18 0.55 | 0.14 0.55 | 0.28 0.55 | 0.28 0.53 | 0.29 0.58 | 0.12 0.44 |
| tile mism. | plants | no no | 0.01 0.00 | 0.05 0.10 | 0.05 0.07 | no no | no no | |
| | embryo | no no | 0.17 0.09 | 0.18 0.16 | 0.25 0.20 | no no | no no | |